

## Predicting the Rossby number in convective experiments

EVAN H. ANDERS,<sup>1,2</sup> CATHRYN M. MANDUCA,<sup>2</sup> BENJAMIN P. BROWN,<sup>1,2</sup> JEFFREY S. OISHI,<sup>3</sup> AND GEOFFREY M. VASIL<sup>4</sup>

<sup>1</sup>*Dept. Astrophysical & Planetary Sciences, University of Colorado – Boulder, Boulder, CO 80309, USA*

<sup>2</sup>*Laboratory for Atmospheric and Space Physics, Boulder, CO 80303, USA*

<sup>3</sup>*Department of Physics and Astronomy, Bates College, Lewiston, ME 04240, USA*

<sup>4</sup>*University of Sydney School of Mathematics and Statistics, Sydney, NSW 2006, Australia*

(Received October 19, 2018; Revised December 10, 2018; Accepted ??)

Submitted to ApJL

### ABSTRACT

The Rossby number is a crucial parameter describing the degree of rotational constraint on the convective dynamics in stars and planets. However, it is not an input to computational models of convection but must be measured ex post facto. Here, we report the discovery of a new quantity, the Predictive Rossby number, which is both tightly correlated with the Rossby number and specified in terms of common inputs to numerical models. The Predictive Rossby number can be specified independent of Rayleigh number, allowing suites of numerical solutions to separate the degree of rotational constraint from the strength of the driving of convection. We examine the scaling of convective transport in terms of the Nusselt number and the degree of turbulence in terms of the Reynolds number of the flow. Finally, we describe the boundary layers as a function of increasing turbulence at constant Rossby number.

*Keywords:* convection — hydrodynamics — turbulence — dynamo — Sun: rotation

### 1. INTRODUCTION

Rotation influences the dynamics of convective flows in stellar and planetary atmospheres. Many studies on the fundamental nature of rotating convection in both laboratory and numerical settings have provided great insight into the properties of convection in both the rapidly rotating regime and the transition to the rotationally unconstrained regime (King et al. 2009; Zhong et al. 2009; Schmitz & Tilgner 2009; King et al. 2012; Julien et al. 2012; King et al. 2013; Ecke & Niemela 2014; Stellmach et al. 2014; Cheng et al. 2015; Gastine et al. 2016) [*Explanation of change: re-arranged and added relevant references*] The scaling behavior of heat transport, the nature of convective flow structures, and the importance of boundary layer-bulk interactions in driving dynamics are well known. Yet, we do not know of any simple procedure for predicting the magnitude of vortical flow gradients purely from experimental con-

trol parameters, such as bulk rotation rate and thermal input.

In the astrophysical context, many studies of rotating convection have investigated questions inspired by the solar dynamo (Glatzmaier & Gilman 1982; Busse 2002; Brown et al. 2008, 2010, 2011; Augustson et al. 2012; Guerrero et al. 2013; Käpylä et al. 2014). Even when these simulations nominally rotate at the solar rate, they frequently produce distinctly different behaviors than the true Sun, such as anti-solar differential rotation profiles (Gastine et al. 2014). It seems that these differences occur because the simulations produce less rotationally constrained states than the Sun. The influence of rotation results from the local shear gradients, and these are not direct input parameters. Recent simulations predict significant rotational influence in the deep solar interior, which can drastically affect flows throughout the solar convection zone (Featherstone & Hindman 2016; Greer et al. 2016). In the planetary context, the balance between magnetic and rotational forces likely leads to the observed differences between ice giant and gas giant dynamos in our solar system (Soderlund et al. 2015). In particular, Aurnou & King (2017) suggest that many

studies of planetary systems have over-emphasized the importance of magnetism compared to rotation.

In short, simulations must achieve the proper rotational balance if they are to explain the behavior of astrophysical objects. ~~(Added: In Boussinesq studies, rotational constraint is often measured by comparing dynamical and thermal boundary layers or deviation in heat transport from the non-rotating state (King et al. 2012; Julien et al. 2012; King et al. 2013). Such measurements are not available for astrophysical objects, where)~~ the degree of rotational influence is best assessed by the ratio between nonlinear advection magnitude and the linear Coriolis accelerations. The *Rossby number* is the standard measure of this ratio,

$$\text{Ro} \equiv \frac{|\nabla \times \mathbf{u}|}{2|\mathbf{\Omega}|} \sim \frac{|(\nabla \times \mathbf{u}) \times \mathbf{u}|}{|2\mathbf{\Omega} \times \mathbf{u}|}, \quad (1)$$

where  $\mathbf{\Omega}$  denotes the bulk rotation vector. Many proxies for the dynamical Rossby number exist that are based solely on input parameters, most notably the *convective* Rossby number. However, all proxies produce imperfect predictions for the true dynamically relevant quantity.

*In this letter, we demonstrate an emperical method of predicting the output Rossby number of convection in a simple stratified system.*

In Anders & Brown (2017) (hereafter AB17), we studied non-rotating compressible convection without magnetic fields in polytropic atmospheres. In this work, we extend AB17 to rotationally-influenced, *f*-plane atmospheres (e.g., Brummell et al. 1996, 1998; Calkins et al. 2015). We determine how the input parameters we studied previously, which controlled the Mach and Reynolds numbers of the evolved flows, couple with the Taylor number (Ta, Julien et al. 1996), which sets the magnitude of the rotational vector.

In section 2, we describe our experiment and paths through parameter space. In section 3, we present the results of our experiments and in section 4 we offer concluding remarks.

## 2. EXPERIMENT

We study fully compressible, stratified convection under precisely the same atmospheric model as in AB17, but here we have included rotation. We study polytropic atmospheres with  $n_p = 3$  density scale heights and a superadiabatic excess of  $\epsilon = 10^{-4}$  such that flows are at low Mach number. We study a domain in which the gravity,  $\mathbf{g} = -g\hat{z}$ , and rotational vector,  $\mathbf{\Omega} = \Omega\hat{z}$ , are antiparallel (as in e.g., Julien et al. 1996; Brummell et al. 1996).

We evolve the velocity ( $\mathbf{u}$ ), temperature ( $T$ ), and log density ( $\ln \rho$ ) according to the Fully Compressible Navier-Stokes equations in the same form presented in AB17, with the addition of the Coriolis term,  $2\mathbf{\Omega} \times \mathbf{u}$ , to the left-hand side of the momentum equation. We impose impenetrable, stress-free, fixed-temperature boundary conditions at the top and bottom of the domain.

We specify the kinematic viscosity ( $\nu$ ), thermal diffusivity ( $\chi$ ), and strength of rotation ( $\Omega$ ) at the top of the domain by choosing the Rayleigh number (Ra), Prandtl number (Pr), and Taylor number (Ta),

$$\text{Ra} = \frac{gL_z^3 \Delta S / c_P}{\nu \chi}, \quad \text{Pr} = \frac{\nu}{\chi}, \quad \text{Ta} = \left( \frac{2\Omega L_z^2}{\nu} \right)^2, \quad (2)$$

where  $L_z$  is the depth of the domain as defined in AB17,  $\Delta S \propto \epsilon n_p$  is the specific entropy difference between ~~(Replaced:  $z = 0$  and  $z = L_z$  replaced with: the top and bottom of the atmosphere)~~, and the specific heat at constant pressure is  $c_P = \gamma/(\gamma - 1)$  with  $\gamma = 5/3$ . Throughout this work we set  $\text{Pr} = 1$ . The Taylor number relates to the often-quoted Ekman number by the equality  $\text{Ek} \equiv \text{Ta}^{-1/2}$ .

~~(Deleted: —The convective Rossby number has provided a common proxy (based on input parameters) for the degree of rotational constraint,~~

~~$\text{Ro}_c = \sqrt{\frac{\text{Ra}}{\text{Pr Ta}}} = \frac{1}{2\Omega} \sqrt{\frac{g \Delta S}{c_P L_z}}$ . This parameter measures the importance of buoyancy relative to rotation without involving dissipation. We show that true Rossby number defined in equation 1 depends nonlinearly on  $\text{Ro}_c$ .— )~~  
~~[Explanation of change: Moved later in section, just above  $\text{Ro}_p$  definition.]~~

The wavenumber of convective onset increases ~~(Replaced: such that,~~ replaced with: ~~according to)~~  $k_{\text{crit}} \propto \text{Ta}^{1/6}$  (Chandrasekhar 1961; Calkins et al. 2015). We study horizontally-periodic, 3D Cartesian ~~(Deleted: convective )~~ domains with extents of  $x, y = [0, 4(2\pi/k_{\text{crit}})]$  and  $z = [0, L_z]$ . At large values of Ta, these domains are tall and skinny, as in Stellmach et al. (2014). We evolve our simulations using the Dedalus<sup>1</sup> pseudospectral framework, and our numerical methods are identical to those presented in AB17.

The critical value of Ra at which convection onsets also depends on Ta (see the black line in figure 1a), roughly according to  $\text{Ra}_{\text{crit}} \sim \text{Ta}^{2/3}$  (Chandrasekhar 1961; Calkins et al. 2015). ~~(Deleted: —We have confirmed these sealings of  $\text{Ra}_{\text{crit}}(\text{Ta})$  and  $k_{\text{crit}}(\text{Ta})$  in our atmospheres using a linear stability analysis.— )~~

<sup>1</sup> <http://dedalus-project.org/>

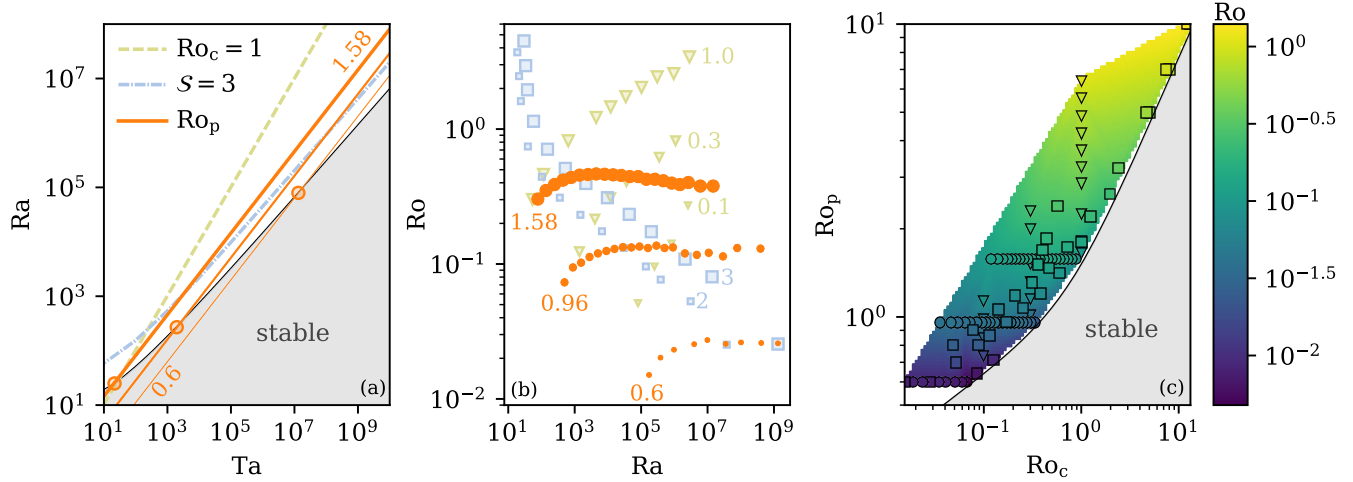


**Figure 1.** (a) The critical Rayleigh number, as a function of the Taylor number, is plotted as a solid black line. The grey shaded region is subcritical, and rotation suppresses convection there. Paths of constant Convective Rossby number ( $Ro_c$ , green dashed line), constant supercriticality ( $S$ , blue dash-dot line), and constant Predictive Rossby number ( $Ro_p$ , orange solid lines) are shown. (Added: From thickest to thinnest, paths with  $Ro_p = [1.58, 0.96, 0.6]$  are plotted, and the value of  $(Ta_{crit}, Ra_{crit})$  for each path is denoted by a circular marker.) (b) Evolved  $Ro$  is plotted vs.  $Ra$  along paths of  $Ro_p = [1.58, 0.96, 0.6]$  for [big, (Added: medium,) small] orange circles. For comparison, paths of constant  $S$  (blue squares,  $S = [3, 2]$  for [big, small] squares) and constant  $Ro_c$  (green triangles,  $Ro_c = [1, 0.3, 0.1]$  for [big, medium, small] triangles) are shown. (Deleted:  $Ro$  is roughly constant for a constant  $Ro_p$ , particularly for the low- $Ro$ ,  $Ro_p = 0.96$  case, but changes drastically at constant  $Ro_c$  or  $S$ .) (c) The evolved value of  $Ro$  is shown as a function of  $Ro_p$  and  $Ro_c$ . Each of the experiments in (b) is outlined by a black (circle, triangle, square) for points along constant  $(Ro_p, Ro_c, S)$  paths. The color inside of the marker represents the exact measured  $Ro$  of that experiment, while the colormap outside of markers is a linear interpolation of the data set. (Deleted: A least-squares fit to all experiments with  $S \geq 1.5$  and  $Ro \geq 0.3$  returns  $Ro = 0.2Ro_c^{-0.19}Ro_p^{1.5}$ . A similar fit to all experiments with  $S \geq 1.5$  and  $Ro < 0.3$  returns  $Ro = 0.1Ro_c^{-0.21}Ro_p^{3.5}$ . In both the high- and low- $Ro$  regime, the measured Rossby number is a strong function of  $Ro_p$  and a weak function of  $Ro_c$ .)

Even taking account of linear theory, the dependence of the evolved nonlinear fluid flows on the input parameters makes predicting the rotational constraint very challenging. We will explore three paths through  $Ra$ - $Ta$  space:

$$Ra = \begin{cases} S Ra_{crit}(Ta), & \text{(I)} \\ (Ro_c)^2 Pr Ta, & \text{(II)} \\ (Ro_p)^2 Pr^{1/2} Ta^{3/4} & \text{(III)}. \end{cases} \quad (3)$$

Paths on constraint I are at constant supercriticality,  $S \equiv Ra/Ra_{crit}$  (blue dash-dot line in figure 1a). Paths on constraint II (Added: (green dashed line in figure 1a)) are at a constant value of the classic convective Rossby number,  $Ro_c$ , which has provided (e.g., Julien et al. 1996; Brummell et al. 1996) a common proxy for the degree of rotational constraint,

$$Ro_c = \sqrt{\frac{Ra}{Pr Ta}} = \frac{1}{2\Omega} \sqrt{\frac{g \Delta S}{c_p L_z}}. \quad (4)$$

This parameter measures the importance of buoyancy relative to rotation without involving dissipation.) (Deleted: It is at a constant value of the classic  $Ro_c$  (green dashed line in figure 1a).) Paths on constraint

III (e.g., orange solid lines in figure 1a) set constant a ratio which we call the “Predictive Rossby number,”

$$Ro_p = \sqrt{\frac{Ra}{Pr^{1/2} Ta^{3/4}}} = \frac{1}{(2\Omega)^{3/4}} \sqrt{\frac{g \Delta S}{c_p \chi^{1/2}}} \quad (5)$$

[Explanation of change: Replaced  $Pr$  with  $Pr^{1/2}$ ; this makes  $Ro_p$  a function of  $\chi$ , rather than  $\nu$ , which better fits the descriptions of thermal boundary layer comparisons that occur later.] (Deleted: Paths along constant  $Ro_c$  are sensitive to the depth of the domain, but are blind to changes in diffusivities with increasing  $Ra$  and  $Ta$ . On the other hand, ) (Added: Unlike paths through parameter space which hold  $Ro_c$  constant,) paths with constant  $Ro_p$  feel changes in diffusivities but not the depth of the domain. To our knowledge, these paths have not been reported in the literature (Added: , although the importance of  $Ra/Ta^{3/4} = Ra Ek^{3/2}$  has been independently found by King et al. (2012) using a boundary layer analysis. We compare our results to their theory in Section 4.)

### 3. RESULTS

(Added: In our stratified domains, for  $Ta \geq 10^5$ , a best-fit to results from a linear stability analysis provides  $Ra_{\text{crit}} = 1.459Ta^{2/3}$  and  $k_{\text{crit}} = 0.414Ta^{1/6}$  for direct onset of convection.) In figure 1a, the value of  $Ra_{\text{crit}}(Ta)$  is shown (Deleted: ~~as a function of  $Ta$~~ ). Sample paths for each criterion in equation 3 through this parameter space are also shown. In figure 1b, we display the evolution of  $Ro$  with increasing  $Ra$  along various paths through parameter space. We find that  $Ro$  increases on constant  $Ro_c$  paths, decreases on constant  $\mathcal{S}$  paths, and remains roughly constant along constant  $Ro_p$  paths. In figure 1c, the value of  $Ro$  is shown simultaneously as a function of  $Ro_p$  and  $Ro_c$  for all experiments conducted in this study. We find a general power-law of the form  $Ro = CRo_c^\alpha Ro_p^\beta$ . (Added: In the rotationally-dominated regime where  $Ro < 0.2$  and  $Re_\perp > 5$  (see Eqn. 8), we find  $\alpha = -0.02$ , and  $Ro$  can be said to be a function of  $Ro_p$  alone. Under this assumption, we report a scaling of  $Ro = (0.148 \pm 0.003)Ro_p^{3.34 \pm 0.07}$ . In the less rotationally dominated regime of  $Ro > 0.2$  and  $Re_\perp > 5$ , we find  $\{C, \alpha, \beta\} = \{0.2, -0.19, 1.5\}$ .) (Deleted: ~~where  $\alpha \approx 3.5$  in the rotationally unconstrained, low- $Ro$  regime and  $\alpha \approx 1.5$  in the unconstrained, high- $Ro$  regime. In the rotationally constrained regime,  $Ro$  is a much stronger function of  $Ro_p$  than  $Ro_c$ , and the evolved  $Ro$  can be approximately determined through specification of  $Ro_p$  alone.~~)

(Deleted: In figure 2, sample snapshots of the evolved entropy field in the  $x-y$  plane near the top of the domain are shown. In the left panel is a rotationally unconstrained flow at moderately high  $Ro$ , and  $Ro$  decreases into the rotationally constrained regime from left to right. As  $Ro$  decreases, the classic granular structure of convection (see e.g., figure 2 in AB17) gives way to vortical columns of convection, as seen in rapidly rotating Rayleigh-Bénard convection (Stellmach et al. 2014). The select cases displayed in figure 2 each have an evolved volume-averaged  $Re \approx 200$ .)

(Added: In figure 2, sample snapshots of the evolved entropy field in the  $x-y$  plane near the top and at the middle of the domain are shown. In the left column, flows are at  $Ro \sim 1$  and resemble the classic granular structure of nonrotating convection (see e.g., figure 2 in AB17), where intense narrow downflow lanes punctuate broad upwellings.  $Ro$  decreases from left to right into the rotationally constrained regime ( $Ro \sim 0.03$ ), in which we observe dynamically persistent, warm upflow columns surrounded by bulk weak downflow regions. These dynamics are similar to those seen in rapidly ro-

tating Rayleigh-Bénard convection (e.g., Stellmach et al. 2014). The select cases displayed in figure 2 each have an evolved volume-averaged  $Re_\perp \approx 32$  (defined below in equation 8).)

We measure the Nusselt number ( $Nu$ ), which quantifies heat transport in a convective solution, as defined in AB17. In figure 3a, we (Replaced: show how  $Nu$  scales replaced with: plot  $Nu$ ) as a function of  $Ra$  (Added:  $/Ra_{\text{crit}}$ ) at fixed  $Ro_p$ . (Deleted: ~~When  $Ro \approx 0.1$ , we find a scaling of  $Nu \propto Ra^{0.27}$ . This is reminiscent of classic scaling laws (e.g.,  $Ra^{2/7}$ ) in non-rotating Rayleigh-Bénard convection (Ahlers et al. 2009). This suggests that changes in heat transport at constant  $Ro_p$  are driven by changes in the thermal boundary layer structure with increasing  $Ra$ .~~) (Added: We find that  $Nu \propto \{Ra^{0.29 \pm 0.01}, Ra^{0.29 \pm 0.01}, Ra^{0.24}\}$  for  $Ro_p = \{0.6, 0.957, 1.58\}$ . These scalings are in line with classic  $2/7$  power law scalings in Rayleigh-Bénard convection (Ahlers et al. 2009), and approach a  $Ra^{1/3}$  scaling, which has been predicted when  $Ro_p$  is held constant (see King et al. 2012, and section 4).)

(Added: Flows are distinctly different parallel to and perpendicular from the rotation vector, which aligns with gravity and stratification. We measure two forms of the RMS Reynolds number,

$$Re_\parallel = \frac{|u|L_z}{\nu}, \quad Re_\perp = \frac{|u|}{\nu} \frac{2\pi}{k_{\text{crit}}}, \quad (6)$$

where the length scale in  $Re_\perp$  is the wavelength of convective onset, and is related to the horizontal extent of our domain (see section 2). From our work in AB17, we expect the RMS velocity to scale as  $|u| \propto \sqrt{\Delta S}$ . By definition,  $\nu \propto \sqrt{Ra/(Pr \Delta S)}$ , and  $L_z$  is a constant set by the stratification while  $k_{\text{crit}} \propto Ta^{1/6}$ . Along paths of constant  $Ro_p$ , we thus expect  $Re_\parallel \propto Ra^{1/2}$  and  $Re_\perp \propto Ra^{5/18}$  when  $Pr$  is held constant.)

In figure 3b, we plot (Replaced: the RMS Reynold's number ( $Re = |u|L_z/\nu$ ) replaced with:  $Re_\parallel$  and  $Re_\perp$ ) as a function of  $Ra$  (Added:  $/Ra_{\text{crit}}$ ) at fixed  $Ro_p$ . (Deleted: ~~, and find that  $Re \propto Ra^{0.47}$  in the rotationally constrained regime, which is almost precisely the  $Re \propto Ra^{1/2}$  scaling measured in the non-rotating regime in AB17.~~) (Added: We find that  $Re_\parallel \propto \{Ra^{0.44 \pm 0.01}, Ra^{0.45 \pm 0.01}, Ra^{0.44}\}$  and  $Re_\perp \propto \{Ra^{0.22 \pm 0.01}, Ra^{0.23 \pm 0.01}, Ra^{0.21}\}$  for  $Ro_p = \{0.6, 0.957, 1.58\}$ . These scalings are similar to but slightly weaker than our predictions in all cases. Furthermore,  $Re_\perp$  collapses for each  $Ro_p$  track, while  $Re_\parallel$  experiences an offset to larger values as  $Ro_p$  shrinks. The offset in  $Re_\parallel$  is unsurprising, because more rotationally constrained flows result in smaller boundary



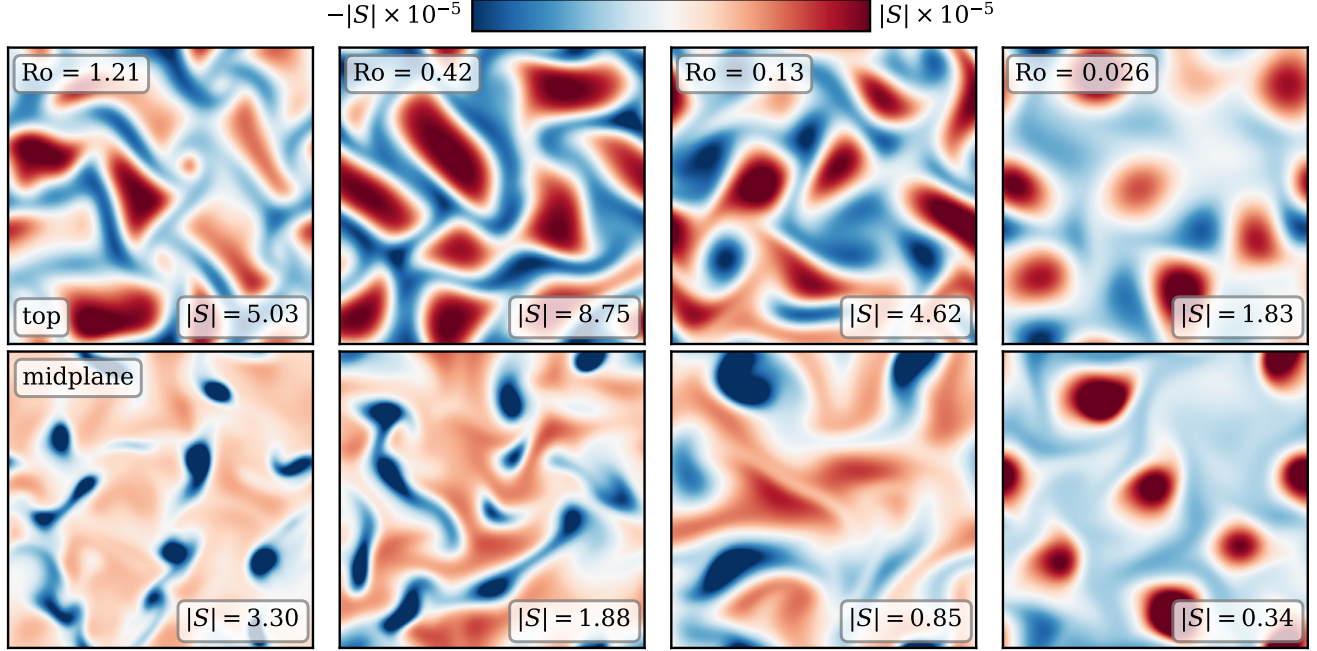


**Figure 2.** Horizontal slice of the evolved entropy (Added: deviation from the mean) (Deleted: field-is-plotted) at  $z = 0.95L_z$  (Added: (top row) and  $z = 0.5L_z$  (bottom row) are shown) for select simulations. (Deleted: The mean value of entropy at this height has been removed in all cases.) All runs displayed here have an evolved volume-averaged  $Re_{\perp} \approx 32$ . As  $Ro$  decreases from  $O(1)$  on the left to  $O(0.03)$  on the right, and thus the rotational constraint on the flow increases, significant changes in flow morphology are observed. (Deleted: At  $Ro = 1.21$  ( $Ro_c = 1$ ), convective dynamics are similar to the non-rotating case where there are large upflows and narrow, fast downflow lanes (see e.g., AB17).) As (Replaced: the rotational constraint increases replaced with:  $Ro$  decreases), (Added: Coriolis forces more effectively deflect the convective flows, and the classic) granular convective pattern gives way to vortical columns.

layers relative to the vertical extent of our stratified domain. The horizontal extent of our domain scales with the strength of rotation, and so regardless of  $Ro_p$ , flows perpendicular to the rotational and buoyant direction are comparably turbulent at the same  $Ra/Ra_{crit}$ . We find  $Re_{\perp}$  and  $Re_{\parallel}$  are, respectively, good proxies for the horizontal and perpendicular resolution required to resolve an experiment.)

Figure 4 shows time- and horizontally-averaged profiles of  $Ro$  and the (Added: standard deviation of the entropy,  $\sigma_s$ .) (Deleted:  $z$ -component of the specific entropy gradient,  $\partial_z s$ .) Figures 4a&b show these profiles for  $Ro_p = 1.58$  ( $Ro \approx 0.4$ ), while Figures 4c&d show these profiles for  $Ro_p = 0.96$  ( $Ro \approx 0.1$ ). The transition in profile behavior from low  $Ra$  (yellow) to high  $Ra$  (purple) is denoted by the color of the profile. As  $Ra$  increases at a constant value of  $Ro_p$ , both the thermal ( $\sigma_s$ ) and dynamical ( $Ro$ ) boundary layers become thinner. We measure the thickness of the thermal boundary layer ( $\delta_s$ ) at the top of the domain by (Added: finding the location of the first maxima of  $\sigma_s$  away from the boundary.) (Deleted: measuring where a linear fit within the boundary layer crosses through

$\partial_z s = 0$ . We ensure by-eye for each profile that this is a reasonable measure of the boundary layer thickness). We measure the thickness of the  $Ro$  boundary layer ( $\delta_{Ro}$ ) (Added: in the same manner.) (Deleted: as the height of the peak value of  $Ro$  within the upper half of the domain.) In figure 4e, we plot  $\delta_{Ro}/\delta_s$ , the ratio of the sizes of these two boundary layers. As anticipated, the dynamical boundary layer ( $\delta_{Ro}$ ) becomes relatively thinner with respect to the thermal boundary layer ( $\delta_s$ ) as  $Ro$  and  $Ro_p$  decrease. (Deleted: At  $Ro_p = 1.58$ , both boundary layers are approximately equally thick, and so both rotational and advective effects are equally important. On the other hand, at  $Ro_p = 0.96$ , the dynamical boundary layer is only 60% the size of the thermal boundary layer, and rotational effects dominate the dynamics.) (Added: However, the precise scaling of this boundary layer ratio with  $Ro_p$  and  $Ra$  is unclear, and we cannot immediately compare these ratios to similar measures from the Rayleigh-Bénard convection literature, such as Fig. 5 of King et al. (2013). They measure the dynamical boundary layer thickness as the peak location of the horizontal velocities, but our horizontal velocities are subject to stress-free boundary

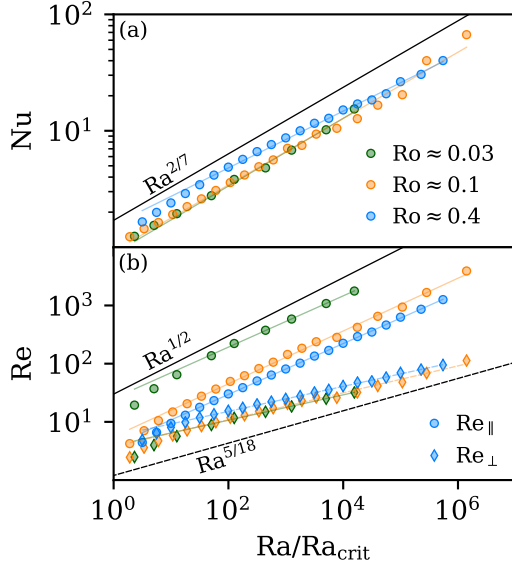


**Figure 3.** (Deleted: -Scaling laws for paths at  $Ro_p = 1.58$  ( $Ro \approx 0.4$ ) and  $Ro_p = 0.96$  ( $Ro \approx 0.1$ ) are shown. — (a) Evolved  $Nu$  vs.  $Ra$ . The scaling laws here are very reminiscent of classic Rayleigh-Bénard convection theory (Ahlers et al. 2009). — (b) Evolved  $Re$  vs.  $Ra$ . The scaling seen here is nearly identical to scalings in nonrotating convection (AB17). —) (Added: Scaling laws for paths at  $Ro_p = 1.58$  ( $Ro \approx 0.4$ ),  $Ro_p = 0.96$  ( $Ro \approx 0.1$ ), and  $Ro_p = 0.6$  ( $Ro \approx 0.03$ ) are shown. Numbers are plotted vs.  $Ra/Ra_{crit}$ , where  $Ra_{crit}$  is the value at which a given  $Ro_p$  path crosses the supercriticality curve (e.g., orange circles in Fig. 1a). (a)  $Nu$ , as defined in AB17, is shown. (b)  $Re_{\parallel}$  and  $Re_{\perp}$ , as defined in equation 8, are shown. All values of  $Ro_p$  trace out similar  $Nu$  and  $Re_{\perp}$  tracks, whereas  $Re_{\parallel}$  tracks shift upwards as  $Ro$  decreases. )

conditions, and we find that the maxima of horizontal velocities occur precisely at the boundaries. In figure 4f, we plot  $\delta_s$  in units of the density scale height at the top of the atmosphere, and we plot vertical lines when this crosses 1. We find no systematic change in behavior when  $\delta_s$  is smaller than the local density scale height.)

#### 4. DISCUSSION

In this letter, we studied low-Mach-number, stratified, compressible convection under the influence of rotation. We examined three paths through  $Ra$ - $Ta$  space, and showed that (Deleted: in the rotationally constrained regime at low  $Ro$ , —) the newly-defined Predictive Rossby number,  $Ro_p = Ra/(Pr^{1/2}Ta^{3/4})$ , determines the value of the evolved Rossby number. (Deleted: While increasing  $Ra$  and holding  $Ro_p$  constant, we find scaling laws of heat transport ( $Nu$ ) and turbulence ( $Re$ ) that are nearly identical to scaling laws seen in nonrotational convection. )

(Added: In this work, we experimentally arrived at the  $Ra/Ta^{3/4} = RaEk^{3/2}$  scaling in  $Ro_p$ , but this relationship was independently discovered by King et al. (2012). Arguing that the thermal boundary layers should scale as  $\delta_s \propto Ra^{-1/3}$  and rotational Ekman boundary layers should scale as  $\delta_{Ro} \propto Ta^{-1/4} = Ek^{1/2}$ , they expect these boundary layers to be equal in size when  $Ra/Ta^{3/4} \sim 1$ . They demonstrate that when  $2 \lesssim Ra/Ta^{3/4} \lesssim 20$  flows are in the transitional regime, and for  $Ra/Ta^{3/4} \lesssim 2$ , flows are rotationally constrained. We note that Boussinesq values of  $Ra$  and  $Ta$  are not the same as their values in our stratified domains here, as diffusivities change with depth (see AB17). Taking into account this change with depth, our simulations fall in King et al. (2012)’s rotationally constrained ( $Ro_p = 0.6$ ) and near-constrained transitional regime ( $Ro_p = \{0.957, 1.58\}$ ). The measured values of  $Ro$  in Fig. 1b and the observed dynamics in Fig. 2 agree with this interpretation.)

We note briefly that the scaling  $Ra \propto Ta^{3/4}$  is very similar to (Replaced: the replaced with: another) theorized boundary between fully rotationally constrained convection and partially constrained convection predicted in Boussinesq theory, of  $Ra \propto Ta^{4/5}$  (Julien et al. 2012; Gastine et al. 2016). This  $Ta^{4/5}$  scaling (Added: also) arises through arguments of geostrophic balance in the boundary layers, and is a steeper scaling than the  $Ta^{3/4}$  scaling present in  $Ro_p$ . This suggests that at sufficiently low  $Ro_p$ , a suite of simulations across many orders of magnitude of  $Ra$  will not only have the same volume-averaged value of  $Ro$  (as in Fig. 1b), but will also maintain proper force balances within the boundary layers.

Our results suggest that by choosing the desired value of  $Ro_p$ , experimenters can select the degree of rotational constraint present in their simulations. (Added: We find that  $Ro \propto Ro_p^{3.34 \pm 0.07}$ , which is within  $2\sigma$  of the estimate in King et al. (2013), who although defining  $Ro$  very differently from our vorticity-based definition here, find  $Ro \propto Ro_p^{3.84 \pm 0.28}$ . We note briefly that they claim that the value of  $Ro$  is strongly dependent upon the Prandtl number studied, and that low  $Ro$  can be achieved at high  $Pr$  without achieving a rotationally constrained flow. We studied only  $Pr = 1$  here, and leave it to future work to determine if the scaling of  $Ro_p \propto Pr^{-1/4}$  is the correct scaling to predict the evolved Rossby number.)

(Added: Despite the added complexity of stratification and despite our using stress-free rather than no-slip boundaries, the boundary layer scaling arguments put forth in King et al. (2012) seem to hold up in our systems. This is reminiscent of what we found in AB17,

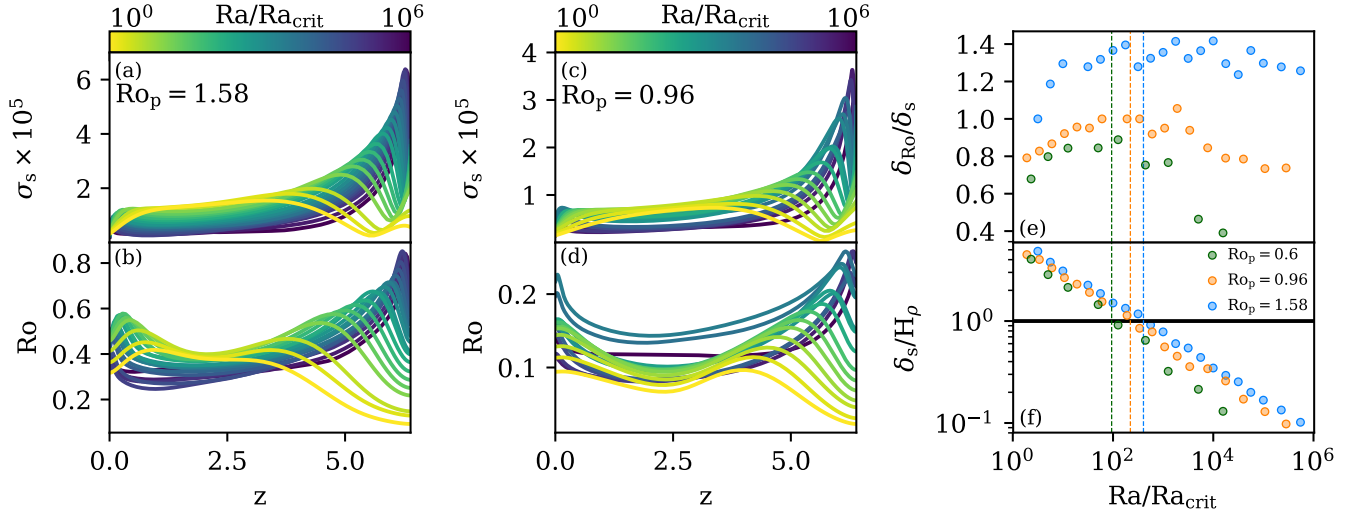


**Figure 4.** Horizontally-averaged profiles of the (~~Replaced:  $z$ -derivative of the specific entropy profile replaced with: standard deviation of entropy~~) ( $\sigma_s$ , a) and Rossby number ( $Ro$ , b) are shown vs. height for  $Ro_p = 1.58$  ( $Ro \approx 0.4$ ). Similar profiles are shown in (c) and (d) for  $Ro_p = 0.96$  ( $Ro \approx 0.1$ ). The color of the profiles denotes the value of  $Ra$  (~~Added:  $/Ra_{crit}$ , where  $Ra_{crit}$  is denoted by an orange circle for each  $Ro_p$  path in Fig. 1a.~~) (~~Deleted:  $-\$ , with yellow profiles being at very low  $Ra$  and purple at the highest values of  $Ra$  studied here.~~) (e) The ratio of the thicknesses of the dynamical boundary layers (~~Added: ( $\delta_{Ro}$ )~~) and thermal boundary layers ( $\delta_s$ ) boundary layers is shown (~~Added: vs.  $Ra/Ra_{crit}$  for fixed  $Ro_p$ .~~) (~~Deleted: for all values of  $Ro_p$  at each value of  $Ra$ . This ratio, and thus the relative importance of both thermal and rotational dynamics, remains roughly constant across orders of magnitude of  $Ra$ .~~) (~~Added: (f) ( $\delta_s$  is plotted vs.  $Ra/Ra_{crit}$  in units of the density scale height at the top of the atmosphere ( $H_\rho$ ). Vertical lines denote when  $\delta_s/H_\rho = 1$  for each value of  $Ro_p$ .~~)

in which convection in stratified domains, regardless of Mach number, produced boundary-layer dominated scaling laws of  $Nu$  that were nearly identical to the scaling laws found in Boussinesq Rayleigh-Bénard convection.)

(~~Added: We close by noting that once  $Ro_p$  is chosen such that a convective system has the same Rossby number as an astrophysical object of choice,~~) it is straightforward to increase the turbulent nature of simulations by increasing  $Ra$ , just as in the non-rotating case. Although all the results reported here are for a Cartesian geometry with antiparallel gravity and rotation, preliminary 3D spherical simulations suggest that  $Ro_p$  also specifies  $Ro$  in more complex geometries (Brown et al. 2019 in prep).

(~~Added: We thank Jon Aurnou and the anonymous referee who independently directed us to the work of King et al. (2012) during the review process, which greatly helped us understand the results of the experiments here. We further thank the anonymous referee for other helpful and clarifying suggestions.~~) This work was supported by NASA Headquarters under the NASA Earth and Space Science Fellowship Program – Grant 80NSSC18K1199. EHA further acknowledges the University of Colorado’s George Ellery Hale Graduate Student Fellowship. This work was additionally supported by NASA LWS grant number NNX16AC92G. Computations were conducted with support by the NASA High End Computing (HEC) Program through the NASA Advanced Supercomputing (NAS) Division at Ames Research Center on Pleiades with allocation GID s1647.

## REFERENCES

- Ahlers, G., Grossmann, S., & Lohse, D. 2009, *Rev. Mod. Phys.*, 81, 503
- Anders, E. H., & Brown, B. P. 2017, *Physical Review Fluids*, 2, 083501
- Augustson, K. C., Brown, B. P., Brun, A. S., Miesch, M. S., & Toomre, J. 2012, *ApJ*, 756, 169
- Aurnou, J. M., & King, E. M. 2017, *Proceedings of the Royal Society of London Series A*, 473, 20160731
- Brown, B. P., Browning, M. K., Brun, A. S., Miesch, M. S., & Toomre, J. 2008, *ApJ*, 689, 1354
- . 2010, *ApJ*, 711, 424
- Brown, B. P., Miesch, M. S., Browning, M. K., Brun, A. S., & Toomre, J. 2011, *ApJ*, 731, 69

- Brummell, N. H., Hurlburt, N. E., & Toomre, J. 1996, *ApJ*, 473, 494
- . 1998, *ApJ*, 493, 955
- Busse, F. H. 2002, *Physics of Fluids*, 14, 1301
- Calkins, M. A., Julien, K., & Marti, P. 2015, *Geophysical and Astrophysical Fluid Dynamics*, 109, 422
- Chandrasekhar, S. 1961, *Hydrodynamic and hydromagnetic stability*
- Cheng, J. S., Stellmach, S., Ribeiro, A., et al. 2015, *Geophysical Journal International*, 201, 1
- Ecke, R. E., & Niemela, J. J. 2014, *PhRvL*, 113, 114301
- Featherstone, N. A., & Hindman, B. W. 2016, *ApJ*, 830, L15
- Gastine, T., Wicht, J., & Aubert, J. 2016, *Journal of Fluid Mechanics*, 808, 690
- Gastine, T., Yadav, R. K., Morin, J., Reiners, A., & Wicht, J. 2014, *MNRAS*, 438, L76
- Glatzmaier, G. A., & Gilman, P. A. 1982, *ApJ*, 256, 316
- Greer, B. J., Hindman, B. W., & Toomre, J. 2016, *ApJ*, 824, 4
- Guerrero, G., Smolarkiewicz, P. K., Kosovichev, A. G., & Mansour, N. N. 2013, *ApJ*, 779, 176
- Julien, K., Knobloch, E., Rubio, A. M., & Vasil, G. M. 2012, *Physical Review Letters*, 109, 254503
- Julien, K., Legg, S., McWilliams, J., & Werne, J. 1996, *Journal of Fluid Mechanics*, 322, 243
- Käpylä, P. J., Käpylä, M. J., & Brandenburg, A. 2014, *A&A*, 570, A43
- King, E. M., Stellmach, S., & Aurnou, J. M. 2012, *Journal of Fluid Mechanics*, 691, 568
- King, E. M., Stellmach, S., & Buffett, B. 2013, *Journal of Fluid Mechanics*, 717, 449
- King, E. M., Stellmach, S., Noir, J., Hansen, U., & Aurnou, J. M. 2009, *Nature*, 457, 301
- Schmitz, S., & Tilgner, A. 2009, *PhRvE*, 80, 015305
- Soderlund, K. M., Sheyko, A., King, E. M., & Aurnou, J. M. 2015, *Progress in Earth and Planetary Science*, 2, 24
- Stellmach, S., Lischper, M., Julien, K., et al. 2014, *PhRvL*, 113, 254501
- Zhong, J.-Q., Stevens, R. J. A. M., Clercx, H. J. H., et al. 2009, *Physical Review Letters*, 102, 044502



---

## List of Changes

---

Added: In Boussinesq studies, rotational constraint is often measured by comparing dynamical and thermal boundary layers or deviation in heat transport from the non-rotating state (King et al. 2012; Julien et al. 2012; King et al. 2013). Such measurements are not available for astrophysical objects, where, on page 2.

Replaced:  $z=0$  and  $z=L_z$  replaced with: the top and bottom of the atmosphere, on page 2.

Deleted: ~~The convective Rossby number has provided a common proxy (based on input parameters) for the degree of rotational constraint,~~

$Ro_c = \sqrt{\frac{Ra}{Pr Ta}} = \frac{1}{2\Omega} \sqrt{\frac{g \Delta S}{c_p L_z}}$ . This parameter measures the importance of buoyancy relative to rotation without involving dissipation. We show that true Rossby number defined in equation 1 depends nonlinearly on  $Ro_c$ . on page 2.

Replaced: ~~such that,~~ replaced with: according to, on page 2.

Deleted: ~~convective~~ on page 2.

Added: From thickest to thinnest, paths with  $Ro_p = [1.58, 0.96, 0.6]$  are plotted, and the value of  $(Ta_{crit}, Ra_{crit})$  for each path is denoted by a circular marker., on page ??.

Added: , 0.6, on page ??.

Added: medium,, on page ??.

Deleted: ~~Ro is roughly constant for a constant  $Ro_p$ , particularly for the low-Ro,  $Ro_p = 0.96$  case, but changes drastically at constant  $Ro_c$  or  $\mathcal{S}$ .~~ on page ??.

Deleted: ~~A least-squares fit to all experiments with  $\mathcal{S} \geq 1.5$  and  $Ro \geq 0.3$  returns  $Ro = 0.2 Ro_c^{-0.19} Ro_p^{1.5}$ . A similar fit to all experiments with  $\mathcal{S} \geq 1.5$  and  $Ro < 0.3$  returns  $Ro = 0.1 Ro_c^{-0.21} Ro_p^{3.5}$ . In both the high- and low-  $Ro$  regime, the measured Rossby number is a strong function of  $Ro_p$  and a weak function of  $Ro_c$ .~~ on page ??.

Added: From thickest to thinnest, paths with  $Ro_p = [1.58, 0.96, 0.6]$  are plotted, and the value of  $(Ta_{crit}, Ra_{crit})$  for each path is denoted by a circular marker., on page 3.

Added: , 0.6, on page 3.

Added: medium,, on page 3.

Deleted: ~~Ro is roughly constant for a constant  $Ro_p$ , particularly for the low-Ro,  $Ro_p = 0.96$  case, but changes drastically at constant  $Ro_c$  or  $\mathcal{S}$ .~~ on page 3.

Deleted: ~~A least-squares fit to all experiments with  $\mathcal{S} \geq 1.5$  and  $Ro \geq 0.3$  returns  $Ro = 0.2 Ro_c^{-0.19} Ro_p^{1.5}$ . A similar fit to all experiments with  $\mathcal{S} \geq 1.5$  and  $Ro < 0.3$  returns  $Ro = 0.1 Ro_c^{-0.21} Ro_p^{3.5}$ . In both the high- and low-  $Ro$  regime, the measured Rossby number is a strong function of  $Ro_p$  and a weak function of  $Ro_c$ .~~ on page 3.

Deleted: ~~We have confirmed these scalings of  $Ra_{crit}(Ta)$  and  $k_{crit}(Ta)$  in our atmospheres using a linear stability analysis.~~ on page 2.

Added: (green dashed line in figure 1a) are at a constant value of the classic *convective* Rossby number,  $Ro_c$ , which has provided (e.g., Julien et al. 1996; Brummell et al. 1996) a common proxy for the degree of rotational constraint,

$$Ro_c = \sqrt{\frac{Ra}{Pr Ta}} = \frac{1}{2\Omega} \sqrt{\frac{g \Delta S}{c_p L_z}}. \quad (7)$$

This parameter measures the importance of buoyancy relative to rotation without involving dissipation., on page 3.

Deleted: ~~It are at a constant value of the classic  $Ro_c$  (green dashed line in figure 1a).~~ on page 3.

Deleted: ~~Paths along constant  $Ro_c$  are sensitive to the depth of the domain, but are blind to changes in diffusivities with increasing  $Ra$  and  $Ta$ . On the other hand,~~ on page 3.

Added: Unlike paths through parameter space which hold  $Ro_c$  constant,, on page 3.

Added: , although the importance of  $Ra/Ta^{3/4} = Ra Ek^{3/2}$  has been independently found by King et al. (2012) using a boundary layer analysis. We compare our results to their theory in Section 4., on page 3.

Added: In our stratified domains, for  $Ta \geq 10^5$ , a best-fit to results from a linear stability analysis provides  $Ra_{\text{crit}} = 1.459Ta^{2/3}$  and  $k_{\text{crit}} = 0.414Ta^{1/6}$  for direct onset of convection., on page 3.

Deleted: ~~as a function of  $Ta$~~  on page 4.

Added: In the rotationally-dominated regime where  $Ro < 0.2$  and  $Re_{\perp} > 5$  (see Eqn. 8), we find  $\alpha = -0.02$ , and  $Ro$  can be said to be a function of  $Ro_p$  alone. Under this assumption, we report a scaling of  $Ro = (0.148 \pm 0.003)Ro_p^{3.34 \pm 0.07}$ . In the less rotationally dominated regime of  $Ro > 0.2$  and  $Re_{\perp} > 5$ , we find  $\{C, \alpha, \beta\} = \{0.2, -0.19, 1.5\}$ ., on page 4.

Deleted: ~~where  $\alpha \approx 3.5$  in the rotationally constrained, low- $Ro$  regime and  $\alpha \approx 1.5$  in the unconstrained, high- $Ro$  regime. In the rotationally constrained regime,  $Ro$  is a much stronger function of  $Ro_p$  than  $Ro_c$ , and the evolved  $Ro$  can be approximately determined through specification of  $Ro_p$  alone.~~ on page 4.

Added: deviation from the mean, on page ??.

Deleted: ~~field is plotted~~ on page ??.

Added: (top row) and  $z = 0.5L_z$  (bottom row) are shown, on page ??.

Deleted: ~~The mean value of entropy at this height has been removed in all cases.~~ on page ??.

Deleted: ~~At  $Ro = 1.21$  ( $Ro_c = 1$ ), convective dynamics are similar to the non-rotating case where there are large upflows and narrow, fast downflow lanes (see e.g., AB17).~~ on page ??.

Replaced: ~~the rotational constraint increases~~ replaced with:  $Ro$  decreases, on page ??.

Added: Coriolis forces more effectively deflect the convective flows, and the classic, on page ??.

Added: deviation from the mean, on page 5.

Deleted: ~~field is plotted~~ on page 5.

Added: (top row) and  $z = 0.5L_z$  (bottom row) are shown, on page 5.

Deleted: ~~The mean value of entropy at this height has been removed in all cases.~~ on page 5.

Deleted: ~~At  $Ro = 1.21$  ( $Ro_c = 1$ ), convective dynamics are similar to the non-rotating case where there are large upflows and narrow, fast downflow lanes (see e.g., AB17).~~ on page 5.

Replaced: ~~the rotational constraint increases~~ replaced with:  $Ro$  decreases, on page 5.

Added: Coriolis forces more effectively deflect the convective flows, and the classic, on page 5.

Deleted: ~~Scaling laws for paths at  $Ro_p = 1.58$  ( $Ro \approx 0.4$ ) and  $Ro_p = 0.96$  ( $Ro \approx 0.1$ ) are shown. (a) Evolved  $Nu$  vs.  $Ra$ . The scaling laws here are very reminiscent of classic Rayleigh-Bénard convection theory (Ahlers et al. 2009). (b) Evolved  $Re$  vs.  $Ra$ . The scaling seen here is nearly identical to scalings in nonrotating convection (AB17).~~ on page ??.

Added: Scaling laws for paths at  $Ro_p = 1.58$  ( $Ro \approx 0.4$ ),  $Ro_p = 0.96$  ( $Ro \approx 0.1$ ), and  $Ro_p = 0.6$  ( $Ro \approx 0.03$ ) are shown. Numbers are plotted vs.  $Ra/Ra_{\text{crit}}$ , where  $Ra_{\text{crit}}$  is the value at which a given  $Ro_p$  path crosses the supercriticality curve (e.g., orange circles in Fig. 1a). (a)  $Nu$ , as defined in AB17, is shown. (b)  $Re_{\parallel}$  and  $Re_{\perp}$ , as defined in equation 8, are shown. All values of  $Ro_p$  trace out similar  $Nu$  and  $Re_{\perp}$  tracks, whereas  $Re_{\parallel}$  tracks shift upwards as  $Ro$  decreases. , on page ??.

Deleted: ~~Scaling laws for paths at  $Ro_p = 1.58$  ( $Ro \approx 0.4$ ) and  $Ro_p = 0.96$  ( $Ro \approx 0.1$ ) are shown. (a) Evolved  $Nu$  vs.  $Ra$ . The scaling laws here are very reminiscent of classic Rayleigh-Bénard convection theory (Ahlers et al. 2009). (b) Evolved  $Re$  vs.  $Ra$ . The scaling seen here is nearly identical to scalings in nonrotating convection (AB17).~~ on page 6.

Added: Scaling laws for paths at  $Ro_p = 1.58$  ( $Ro \approx 0.4$ ),  $Ro_p = 0.96$  ( $Ro \approx 0.1$ ), and  $Ro_p = 0.6$  ( $Ro \approx 0.03$ ) are shown. Numbers are plotted vs.  $Ra/Ra_{\text{crit}}$ , where  $Ra_{\text{crit}}$  is the value at which a given  $Ro_p$  path crosses the supercriticality curve (e.g., orange circles in Fig. 1a). (a)  $Nu$ , as defined in AB17, is shown. (b)  $Re_{\parallel}$  and  $Re_{\perp}$ , as defined in equation 8, are shown. All values of  $Ro_p$  trace out similar  $Nu$  and  $Re_{\perp}$  tracks, whereas  $Re_{\parallel}$  tracks shift upwards as  $Ro$  decreases. , on page 6.

Replaced:  ~~$z$ -derivative of the specific entropy profile~~ replaced with: standard deviation of entropy, on page ??.

Added:  $/Ra_{\text{crit}}$ , where  $Ra_{\text{crit}}$  is denoted by an orange circle for each  $Ro_p$  path in Fig. 1a., on page ??.

Deleted: ~~, with yellow profiles being at very low  $Ra$  and purple at the highest values of  $Ra$  studied here.~~ on page ??.

Added:  $(\delta_{Ro})$ , on page ??.

Added: vs.  $Ra/Ra_{\text{crit}}$  for fixed  $Ro_p$ , on page ??.

Deleted: ~~for all values of  $Ro_p$  at each value of  $Ra$ . This ratio, and thus the relative importance of both thermal and rotational dynamics, remains roughly constant across orders of magnitude of  $Ra$ .~~ on page ??.

Added: (f)  $\delta_s$  is plotted vs.  $Ra/Ra_{\text{crit}}$  in units of the density scale height at the top of the atmosphere ( $H_\rho$ ). Vertical lines denote when  $\delta_s/H_\rho = 1$  for each value of  $Ro_p$ , on page ??.

Replaced:  ~~$z$ -derivative of the specific entropy profile~~ replaced with: standard deviation of entropy, on page 7.

Added:  $/Ra_{\text{crit}}$ , where  $Ra_{\text{crit}}$  is denoted by an orange circle for each  $Ro_p$  path in Fig. 1a., on page 7.

Deleted: ~~, with yellow profiles being at very low  $Ra$  and purple at the highest values of  $Ra$  studied here.~~ on page 7.

Added: ( $\delta_{Ro}$ ), on page 7.

Added: vs.  $Ra/Ra_{\text{crit}}$  for fixed  $Ro_p$ , on page 7.

Deleted: ~~for all values of  $Ro_p$  at each value of  $Ra$ . This ratio, and thus the relative importance of both thermal and rotational dynamics, remains roughly constant across orders of magnitude of  $Ra$ .~~ on page 7.

Added: (f)  $\delta_s$  is plotted vs.  $Ra/Ra_{\text{crit}}$  in units of the density scale height at the top of the atmosphere ( $H_\rho$ ). Vertical lines denote when  $\delta_s/H_\rho = 1$  for each value of  $Ro_p$ , on page 7.

Deleted: ~~In figure 2, sample snapshots of the evolved entropy field in the  $x-y$  plane near the top of the domain are shown. In the left panel is a rotationally unconstrained flow at moderately high  $Ro$ , and  $Ro$  decreases into the rotationally constrained regime from left to right. As  $Ro$  decreases, the classic granular structure of convection (see e.g., figure 2 in AB17) gives way to vortical columns of convection, as seen in rapidly rotating Rayleigh-Bénard convection (Stellmach et al. 2014). The select cases displayed in figure 2 each have an evolved volume-averaged  $Re \approx 200$ .~~ on page 4.

Added: In figure 2, sample snapshots of the evolved entropy field in the  $x-y$  plane near the top and at the middle of the domain are shown. In the left column, flows are at  $Ro \sim 1$  and resemble the classic granular structure of nonrotating convection (see e.g., figure 2 in AB17), where intense narrow downflow lanes punctuate broad upwellings.  $Ro$  decreases from left to right into the rotationally constrained regime ( $Ro \sim 0.03$ ), in which we observe dynamically persistent, warm upflow columns surrounded by bulk weak downflow regions. These dynamics are similar to those seen in rapidly rotating Rayleigh-Bénard convection (e.g., Stellmach et al. 2014). The select cases displayed in figure 2 each have an evolved volume-averaged  $Re_\perp \approx 32$  (defined below in equation 8), on page 4.

Replaced: ~~show how  $Nu$  scales~~ replaced with: plot  $Nu$ , on page 4.

Added:  $/Ra_{\text{crit}}$ , on page 4.

Deleted: ~~When  $Ro \approx 0.1$ , we find a scaling of  $Nu \propto Ra^{0.27}$ . This is reminiscent of classic scaling laws (e.g.,  $Ra^{2/7}$ ) in non-rotating Rayleigh-Bénard convection (Ahlers et al. 2009). This suggests that changes in heat transport at constant  $Ro_p$  are driven by changes in the thermal boundary layer structure with increasing  $Ra$ .~~ on page 4.

Added: We find that  $Nu \propto \{Ra^{0.29 \pm 0.01}, Ra^{0.29 \pm 0.01}, Ra^{0.24}\}$  for  $Ro_p = \{0.6, 0.957, 1.58\}$ . These scalings are in line with classic  $2/7$  power law scalings in Rayleigh-Bénard convection (Ahlers et al. 2009), and approach a  $Ra^{1/3}$  scaling, which has been predicted when  $Ro_p$  is held constant (see King et al. 2012, and section 4), on page 4.

Added: Flows are distinctly different parallel to and perpendicular from the rotation vector, which aligns with gravity and stratification. We measure two forms of the RMS Reynolds number,

$$Re_\parallel = \frac{|u|L_z}{\nu}, \quad Re_\perp = \frac{|u|}{\nu} \frac{2\pi}{k_{\text{crit}}}, \quad (8)$$

where the length scale in  $Re_\perp$  is the wavelength of convective onset, and is related to the horizontal extent of our domain (see section 2). From our work in AB17, we expect the RMS velocity to scale as  $|u| \propto \sqrt{\Delta S}$ . By definition,  $\nu \propto \sqrt{Ra/(\text{Pr} \Delta S)}$ , and  $L_z$  is a constant set by the stratification while  $k_{\text{crit}} \propto \text{Ta}^{1/6}$ . Along paths of constant  $Ro_p$ , we thus expect  $Re_\parallel \propto Ra^{1/2}$  and  $Re_\perp \propto Ra^{5/18}$  when  $\text{Pr}$  is held constant., on page 4.

Replaced: ~~the RMS Reynold's number ( $Re = |u|L_z/\nu$ )~~ replaced with:  $Re_\parallel$  and  $Re_\perp$ , on page 4.

Added:  $/Ra_{\text{crit}}$ , on page 4.

Deleted: ~~, and find that  $Re \propto Ra^{0.47}$  in the rotationally constrained regime, which is almost precisely the  $Re \propto Ra^{1/2}$  scaling measured in the non-rotating regime in AB17.~~ on page 4.

Added: We find that  $Re_{\parallel} \propto \{Ra^{0.44 \pm 0.01}, Ra^{0.45 \pm 0.01}, Ra^{0.44}\}$  and  $Re_{\perp} \propto \{Ra^{0.22 \pm 0.01}, Ra^{0.23 \pm 0.01}, Ra^{0.21}\}$  for  $Ro_p = \{0.6, 0.957, 1.58\}$ . These scalings are similar to but slightly weaker than our predictions in all cases. Furthermore,  $Re_{\perp}$  collapses for each  $Ro_p$  track, while  $Re_{\parallel}$  experiences an offset to larger values as  $Ro_p$  shrinks. The offset in  $Re_{\parallel}$  is unsurprising, because more rotationally constrained flows result in smaller boundary layers relative to the vertical extent of our stratified domain. The horizontal extent of our domain scales with the strength of rotation, and so regardless of  $Ro_p$ , flows perpendicular to the rotational and buoyant direction are comparably turbulent at the same  $Ra/Ra_{crit}$ . We find  $Re_{\perp}$  and  $Re_{\parallel}$  are, respectively, good proxies for the horizontal and perpendicular resolution required to resolve an experiment., on page 4.

Added: standard deviation of the entropy,  $\sigma_s$ ., on page 5.

Deleted: ~~z-component of the specific entropy gradient,  $\partial_z s$ .~~ on page 5.

Added: finding the location of the first maxima of  $\sigma_s$  away from the boundary., on page 5.

Deleted: ~~measuring where a linear fit within the boundary layer crosses through  $\partial_z s = 0$ . We ensure by-eye for each profile that this is a reasonable measure of the boundary layer thickness~~ on page 5.

Added: in the same manner., on page 5.

Deleted: ~~as the height of the peak value of  $Ro$  within the upper half of the domain.~~ on page 5.

Deleted: ~~At  $Ro_p = 1.58$ , both boundary layers are approximately equally thick, and so both rotational and advective effects are equally important. On the other hand, at  $Ro_p = 0.96$ , the dynamical boundary layer is only 60% the size of the thermal boundary layer, and rotational effects dominate the dynamics.~~ on page 5.

Added: However, the precise scaling of this boundary layer ratio with  $Ro_p$  and  $Ra$  is unclear, and we cannot immediately compare these ratios to similar measures from the Rayleigh-Bénard convection literature, such as Fig. 5 of King et al. (2013). They measure the dynamical boundary layer thickness as the peak location of the horizontal velocities, but our horizontal velocities are subject to stress-free boundary conditions, and we find that the maxima of horizontal velocities occur precisely at the boundaries. In figure 4f, we plot  $\delta_s$  in units of the density scale height at the top of the atmosphere, and we plot vertical lines when this crosses 1. We find no systematic change in behavior when  $\delta_s$  is smaller than the local density scale height., on page 5.

Deleted: ~~in the rotationally constrained regime at low  $Ro$ .~~ on page 6.

Deleted: ~~While increasing  $Ra$  and holding  $Ro_p$  constant, we find scaling laws of heat transport ( $Nu$ ) and turbulence ( $Re$ ) that are nearly identical to scaling laws seen in nonrotational convection.~~ on page 6.

Added: In this work, we experimentally arrived at the  $Ra/Ta^{3/4} = Ra Ek^{3/2}$  scaling in  $Ro_p$ , but this relationship was independently discovered by King et al. (2012). Arguing that the thermal boundary layers should scale as  $\delta_S \propto Ra^{-1/3}$  and rotational Ekman boundary layers should scale as  $\delta_{Ro} \propto Ta^{-1/4} = Ek^{1/2}$ , they expect these boundary layers to be equal in size when  $Ra/Ta^{3/4} \sim 1$ . They demonstrate that when  $2 \lesssim Ra/Ta^{3/4} \lesssim 20$  flows are in the transitional regime, and for  $Ra/Ta^{3/4} \lesssim 2$ , flows are rotationally constrained. We note that Boussinesq values of  $Ra$  and  $Ta$  are not the same as their values in our stratified domains here, as diffusivities change with depth (see AB17). Taking into account this change with depth, our simulations fall in King et al. (2012)'s rotationally constrained ( $Ro_p = 0.6$ ) and near-constrained transitional regime ( $Ro_p = \{0.957, 1.58\}$ ). The measured values of  $Ro$  in Fig. 1b and the observed dynamics in Fig. 2 agree with this interpretation., on page 6.

Replaced: ~~the~~ replaced with: another, on page 6.

Added: also, on page 6.

Added: We find that  $Ro \propto Ro_p^{3.34 \pm 0.07}$ , which is within  $2\sigma$  of the estimate in King et al. (2013), who although defining  $Ro$  very differently from our vorticity-based definition here, find  $Ro \propto Ro_p^{3.84 \pm 0.28}$ . We note briefly that they claim that the value of  $Ro$  is strongly dependent upon the Prandtl number studied, and that low  $Ro$  can be achieved at high  $Pr$  without achieving a rotationally constrained flow. We studied only  $Pr = 1$  here, and leave it to future work to determine if the scaling of  $Ro_p \propto Pr^{-1/4}$  is the correct scaling to predict the evolved Rossby number., on page 6.

Added: Despite the added complexity of stratification and despite our using stress-free rather than no-slip boundaries, the boundary layer scaling arguments put forth in King et al. (2012) seem to hold up in our systems. This is reminiscent of what we found in AB17, in which convection in stratified domains, regardless of Mach number, produced boundary-

layer dominated scaling laws of  $Nu$  that were nearly identical to the scaling laws found in Boussinesq Rayleigh-Bénard convection., on page 6.

Added: We close by noting that once  $Ro_p$  is chosen such that a convective system has the same Rossby number as an astrophysical object of choice,, on page 7.

Added: We thank Jon Aurnou and the anonymous referee who independently directed us to the work of King et al. (2012) during the review process, which greatly helped us understand the results of the experiments here. We further thank the anonymous referee for other helpful and clarifying suggestions., on page 7.